Lawrence Berkeley National Laboratory

Title

First of Their Kind: Solar Cells with a Dry-Processed Perovskite Absorber Layer via Powder Aerosol Deposition and Hot-Pressing

Permalink

https://escholarship.org/uc/item/16f3727f

Journal

Solar RRL, 7(16)

ISSN

2367–198X

Authors

Biberger, Simon
Leupold, Nico
Witt, Christina
et al.

Publication Date

2023-08-01

DOI

10.1002/solr.202300261

Peer reviewed

First of Their Kind: Solar Cells with a Dry-Processed Perovskite Absorber Layer via Powder Aerosol Deposition and Hot-Pressing

Simon Biberger, Nico Leupold, Christina Witt, Christopher Greve, Paul Markus, Philipp Ramming, Daniel Lukas, Konstantin Schötz, Frank-Julian Kahle, Chenhui Zhu, Georg Papastavrou, Anna Köhler, Eva M. Herzig, Ralf Moos, and Fabian Panzer*

Preparing halide perovskite films by solvent-free, powder-based processing approaches currently attracts more and more attention. However, working solar cells employing dry, powder-based halide perovskite thin films, have not been demonstrated so far. Herein, perovskite solar cells are presented where the absorber layer is prepared by transferring readily synthesized perovskite powders into a compact thin film using a fully dry-powder-processing concept. Compact thin films are deposited via an optimized powder aerosol deposition (PAD) process. Pressing at 120 °C further improves the morphology and the optoelectronic film properties. Integrating the perovskite films in a solar cell configuration results in fully working devices, with champion power conversion efficiencies of >6%. While the (optoelectronic) properties of the PAD-processed films are found to be comparable with their solution-processed counterparts, investigations of the solar cell stack suggest deterioration of the electron-transport layer properties due to the PAD process, and the presence of hydrates at the perovskite surface to be important factors that contribute to the limited solar cell efficiency. Herein, perspectives to overcome the identified limitations are outlined, emphasizing the high potential and realizability of efficient perovskite solar cells based on dry-powder-processing approaches in the future.

1. Introduction

Within the last decade, the rise of metal-halide perovskites (MHP) as light absorber in solar cells has been remarkable. Power conversion efficiencies (PCEs) of up to 25.7%[1,2] and increasing device stabilities of up to several thousand hours[3,4] currently push perovskite solar cells on the verge to commercialization.

For high PCEs however, high-quality MHP films are required. Most of such high-quality perovskite films are currently prepared either by solution-based processing or evaporation methods.[2,4–6] Despite their widespread application in perovskite film fabrication, these approaches are still facing limitations.

One inherent limitation of solution-based and evaporation methods is the intrinsic coupling between perovskite synthesis and film formation, rendering the morphology and final optoelectronic functionality of perovskite films to be extremely sensitive to the precise processing conditions.[7–10] Moreover, a second drawback of solution-based processing is the need for toxic solvents such as dimethylfluorene (DMF)[11,12] to prepare the precursor

S. Biberger, C. Witt, P. Ramming, K. Schötz, F.-J. Kahle, A. Köhler, F. Panzer
Soft Matter Optoelectronics (EP II)
University of Bayreuth
95440 Bayreuth, Germany
E-mail: fabian.panzer@uni-bayreuth.de

N. Leupold, D. Lukas, R. Moos
Department of Functional Materials
University of Bayreuth
95440 Bayreuth, Germany

C. Greve, E. M. Herzig
Dynamics and Structure Formation - Herzig Group
University of Bayreuth
95440 Bayreuth, Germany

P. Markus, G. Papastavrou
Physical Chemistry II
University of Bayreuth
95440 Bayreuth, Germany

C. Zhu
Advanced Light Source
Lawrence Berkeley National Lab
Berkeley, CA 94720, USA

stock solutions. Replacing these toxic solvents was already subject of several studies with the aim to find greener alternatives for perovskite stock solutions.[13–16]

An attractive film-processing approach, which does not rely on solvents and that decouples the perovskite synthesis and film formation, is the dry processing of already synthesized MHP powders via powder aerosol deposition (PAD).[17–19] Here, an aerosol is generated from powder and accelerated onto a substrate, where the powder particles break up and form a dense film. PAD is well established for a variety of different ceramic materials, like technical ceramics,[20–23] and ceramics for sensing and energy applications.[24] First commercial applications of PAD are already tested.[25]

Using a basic PAD setup, we showed in a previous work that thin films of MHPs such as the model perovskite methylammonium lead iodide (MAPbI$_3$) can be produced via PAD.[26] Yet, clear improvements in film morphology (compactness, surface roughness) were still required to realize film properties suitable for applications in optoelectronic thin film devices, such as perovskite solar cells.

In the past, it was demonstrated that the compactness and surface roughness of MHP can be improved by pressure treatment.[27–30] In addition, it became clear that performing the pressure treatment under elevated temperature not only further improved the surface roughness and the compactness, but even led to enlarged grain sizes, which is known to be beneficial regarding the MHP's optoelectronic functionality.[31–34]

Here, we present sophisticated technical developments in the PAD process that enable the deposition of thin (≈1 μm), yet dense MAPbI$_3$ films. In addition, we successfully employ pressure treatment of the optimized PAD films to further improve morphology and optoelectronic properties.

With these improvements, we demonstrate the first realization of pressed and unpressed PAD-processed MAPbI$_3$ thin films in a solar cell configuration, resulting in fully working devices with PCEs of >6%. We highlight in detail the challenges that remain and discuss approaches to tackle the current limitations to manufacture highly efficient solar cells in the future based on the here presented novel perovskite-processing method.

2. Process Development toward Dry-Processed Perovskite Absorber Layers Suitable for the Use in PSCs

2.1. PSC Fabrication Concept

The fabrication process of our perovskite solar cells with a completely dry, powder-based perovskite-processing approach is presented in **Figure 1**. First, we synthesize MAPbI$_3$ powder mechanochemically via ball milling (details in previous work[35,36]), and use this powder in a dry PAD process.

A PAD system consists of three main components: 1) a vacuum pump for generating a rough vacuum with an absolute pressure in the range of 1 mbar, 2) a deposition chamber in which the substrate is mounted on a movable substrate holder, and 3) an aerosol generating unit (Figure S1, Supporting Information). In the latter, a powder aerosol is generated from the dry mechanochemically synthesized powder by passing a carrier gas such as N$_2$, O$_2$, or He, for example, through a powder bed located on a porous tray in a glass flask.

The powder aerosol is transported from the aerosol generating unit to the evacuated deposition chamber due to the pressure difference between both components. In the deposition chamber, the powder aerosol is further accelerated through a nozzle to velocities between 100 and 600 m s^{-1} and directed onto a glass substrate coated with indium tin oxide (ITO) as transparent electrode and SnO$_2$ as electron-transport layer (ETL).

Upon impact on the substrate, the powder particles in the aerosol deform, break up, and adhere to the substrate. Subsequently impacting particles increase the film thickness, further fragment previously deposited particles and densify the film. This mechanism is called room-temperature impact consolidation (RTIC).[37] The MAPbI$_3$ films, deposited via the PAD approach (further referred to as pristine films), are dense, fully covering the substrate (Figure S11, Supporting Information). To reduce the surface roughness and further improve the film quality of the pristine MAPbI$_3$ PAD films, we applied hot-pressing as an optional posttreatment step before spin-coating 2,2′,7,7′-Tetrakis[N,N-di(4-methoxyphenyl)amino]-9,9′-spirobifluorene (spiro-MeOTAD) as hole-transport layer (HTL) onto the MAPbI$_3$ film and thermally evaporating gold as top electrode to complete the solar cells.
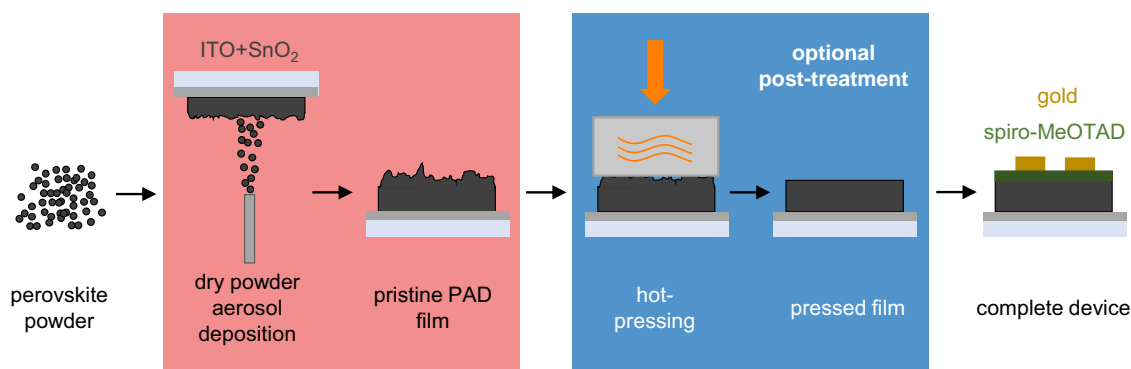

Figure 1. Fabrication concept for a solar cell with a perovskite absorber layer processed via the powder aerosol deposition (PAD) method and optional subsequent hot-pressing.

In the following, we first describe the key improvements in the PAD process that allow for successful fabrication of compact perovskite films with thicknesses in the range of ≈1 µm (Section 2.2.). Then, we outline relevant aspects in the hot-pressing step of the PAD perovskite films (Section 2.3) and discuss the properties of the fully dry-processed powder-based perovskite solar cells in Section 3.

2.2. Key Improvements in the PAD Process

In general, the powder particle size and the presence of agglomerates consisting of those powder particles are decisive for the film formation during PAD. Desired particle sizes are typically in the range between 200 nm to 5 µm.[38] Due to their low mass, smaller particles exhibit low kinetic energy and inertia so that they either do not reach the substrate or bounce off the substrate upon impact. In contrast, too high kinetic energy of larger particles can result in abrasion of the substrate, similar to sandblasting.[38]

The presence of large agglomerates in the PAD process is also detrimental to the film properties, as a large fraction of their kinetic energy is used to break up the initially large agglomerates into smaller agglomerates and individual powder particles when impacting the substrate. Thus, less energy is available for deforming and fracturing the individual particles as necessary for densification of the film via RTIC.[38] As a result, porous films with voids (pinholes through the whole film thickness) and bad contact to the substrate (Figure S2, Supporting Information) are deposited. Thus, the aerosol generation, that is, especially the reduction of the number of agglomerates within the powder aerosol, is a key to allow for PAD-deposited MAPbI$_3$ thin films suitable for solar cells.

Our mechanochemically synthesized powder used for PAD is phase pure und consists of 30–50 µm large agglomerates of powder particles in the 1 µm range (Figure S3 and S4, Supporting Information). While the powder particle size is well suitable for PAD, size and number of agglomerates impacting on the substrate have to be reduced to obtain high-quality PAD films. To fragment the agglomerates before they reach the substrate, we implemented an ejector unit after the aerosol flask. The ejector consists of 1) a horizontal tube, whose cross section narrows at a throat and expands afterward and 2) a second tube, that enters the first tube perpendicular in the expansion zone (Figure 2a).

The ejector unit serves two beneficial purposes. First, strong shear forces are present when $\dot{V}_{acc}$ (gas flow for acceleration of aerosol) and $\dot{V}_{flask}$ (gas flow of carrier gas for aerosol generation in the flask) are merging perpendicular to each other after the throat in the ejector unit. In addition, agglomerates accelerate upon entering the gas flow $\dot{V}_{total}$ (Figure 2a). Both effects contribute to break up agglomerates within the aerosol.[39] The second advantage of the ejector is the possibility to independently control $\dot{V}_{flask}$ and $\dot{V}_{acc}$. This allows to apply a low $\dot{V}_{flask}$, and thus to reduce the overall MAPbI$_3$ aerosol concentration significantly. Consequently, while more passes, that is, a higher number of movements of the substrate over the nozzle, are necessary to realize a certain film thickness, fluctuations in the aerosol concentration are much better compensated, compared to a PAD setup without ejector unit. This eventually allows for producing PAD films with more homogeneous film coverage. In passing, we note that replacing the ejector with a simple tee to reduce the complexity of the setup does not result in satisfying film quality (Figure S5, Supporting Information).

Figure 2b, top panel, shows a scanning electron microscope (SEM) image of a MAPbI$_3$ PAD film deposited using the ejector. The film is compact with only small pores and has an overall good contact to the bottom layer. Yet, even with the ejector, the MAPbI$_3$ PAD films still exhibit voids (Figure 2b top). In addition, the film area deposited from the middle of the 10 mm slit nozzle is thicker compared to the area from the edges of the nozzle. This inhomogeneity in film thickness indicates that agglomerates are still present in the aerosol, most likely in the center of the aerosol jet hitting the substrate. An explanation of this observation is that agglomerates do not follow the gas flow due to their large inertia when the circular cross section of the tube leading the gas flow to the nozzle changes from a diameter of 4 mm to a slit orifice of 10 mm × 0.5 mm of the nozzle.

To finally remove these persisting agglomerates from the aerosol, we employed an inertial separator unit, consisting of a tee and a tube between the ejector and slit nozzle (Figure 2a). In the inertial separator, the aerosol jet coming from the ejector is deflected by 90° and directed to the slit nozzle. Consequently,
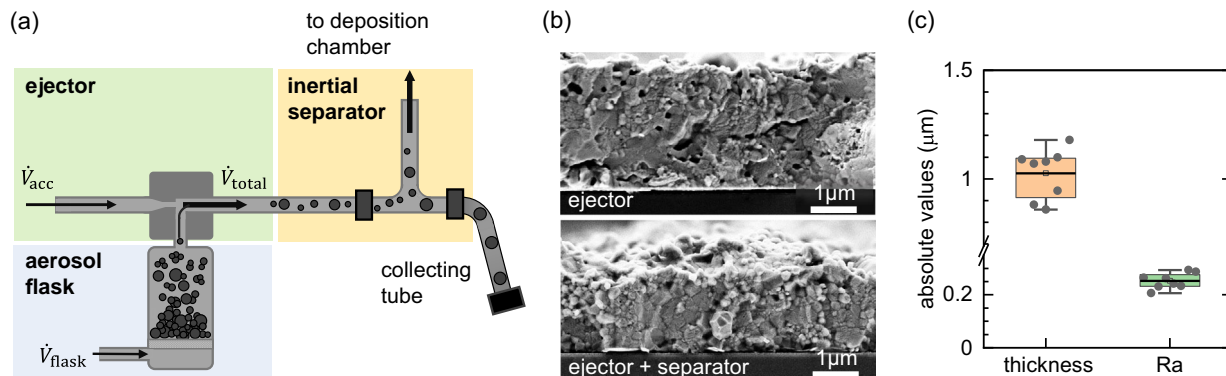

Figure 2. a) Concept of the improved aerosol generation employing an ejector unit and inertial separator. b) Scanning electron microscope (SEM) cross-section images of PAD films deposited with ejector (top) and with ejector and inertial separator (bottom). c) Resulting thickness and surface roughness Ra of the optimized pristine PAD films deposited with ejector and inertial separator.

only smaller agglomerates and particles in the aerosol jet can follow the gas flow to the nozzle, while larger agglomerates end up in the collecting tube due to their larger inertia.

In passing, we mention that in addition to these technical improvements addressing the agglomerates issue, we also integrated a smaller flask with a diameter of 3 cm in the aerosol generation unit allowing to use low powder quantities (<1 g) to further reduce the aerosol concentration and increase the general process control.

By these setup improvements, we obtain dense and void-free $MAPbI_3$ films (Figure 2b bottom) with mean thickness of (1.0 ± 0.1) μm and reasonable arithmetic mean roughness Ra of (0.25 ± 0.03) μm (Figure 2c, for details about chosen PAD process parameters, see Section S1, Supporting Information). Thus, the modified aerosol generation with ejector and inertial separator allows to deposit 1 μm thick $MAPbI_3$ films from highly agglomerated powders with, considering the field of PAD, high reproducibility.

2.3. Posttreatment via Hot-Pressing

Pressing at elevated temperature has emerged as powerful technique to improve $MAPbI_3$ film properties, that is, film morphology, optoelectronic properties, as well as related solar cell efficiencies.[31–34,40–42] In particular, a higher pressure–temperature combination is known to result in stronger improvements of $MAPbI_3$ film morphology and optoelectronic properties.[27,28,31–33,40,41,43] To further improve the perovskite film quality of the pristine PAD films, we therefore applied an additional hot-pressing posttreatment step.

First, we explored the possibility to employ press die materials commonly used for pressing MHP films. While silicon wafers and PTFE sheets were often used in the past,[31,33,34,40–45] their form stability is limited to pressures below 15 MPa in single action pressing.[31,34,40,41,44] To achieve clear improvements upon pressure treatment of our PAD films, we aimed for a pressure of 25 MPa, rendering silicon wafers and PTFE sheets unsuited for our approach. Polyimide foil exhibits high form stability under mechanical and thermal stress,[46] and was already used as press die material for the fabrication of MHP films with promising

optoelectronic properties in the past.[47,48] We examined polyimide foil as press die material in our press setup but observed that after pressing the polyimide foil exhibited significant wear and the PAD film tended to stick to the polyimide foil (for detailed discussion, see Figure S6, Supporting Information).

Due to these issues, we explored the possibility to use glass blocks (thickness: 8 mm, roughness: 2 nm) as press die material, covered with a silanization coating (trichloro(octadecyl)silane in toluene from liquid phase) to prevent the glass blocks from sticking to the perovskite film. Using the silanized glass blocks, our PAD films can be pressed reliably and without breakage of glass substrates and glass blocks employing up to 25 MPa at 120 °C for 5 min. For our experiments, we thus choose this set of process parameters, as it is known that increased temperature and pressure are beneficial for improving the morphology and optoelectronic properties when pressing halide perovskite films[27,28,31–33,40,41,43] (also see Figure S7, Supporting Information, and previous work[28] for details on press setup and protocol).

Applying this pressing procedure to the pristine PAD films, which appear matt black before pressing, we obtain shiny gray films after the pressing step (**Figure 3**b left). This change in optical appearance already indicates a reduction in surface roughness, which is further evidenced from the comparison of top-view SEM images of a pressed film and a pristine film (Figure 3b right). We quantified the mean Ra value of the pressed films to be 18 nm, compared to 250 nm of the pristine films, confirming a reduction in surface roughness by >92% upon pressing (Figure 3c). Additionally, pressing the PAD films with 25 MPa at 120 °C reduced the film thickness by about 37% (Figure 3c), indicating an increased compaction of the pressed $MAPbI_3$ films. More details on the changes of morphology and optoelectronic properties of pristine and pressed $MAPbI_3$ films are discussed in Section 4.2.

In summary, by employing the previously described key developments in the PAD process, in combination with an optional hot-pressing step of the pristine PAD perovskite films, we demonstrated the successful production of phase pure and dense polycrystalline $MAPbI_3$ thin films that meet the film requirements for the use in functional perovskite solar cells.
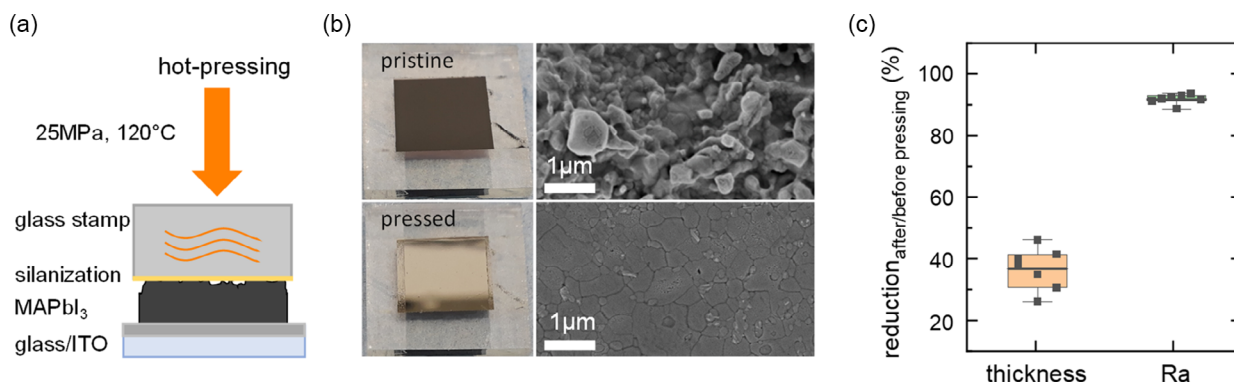

Figure 3. a) Sketch of hot-pressing a PAD film. b) Photographs (left) and top-view SEM images (right) of pristine (top) and pressed (bottom) $MAPbI_3$ PAD films. c) Reduction of thickness and surface roughness (Ra) of PAD films due to pressing (see Figure S8, Supporting Information, for absolute values).

3. Solar Cells

Based on the described process improvements and following the concept in Figure 1, we manufactured two types of complete solar cell stacks. One type uses a pristine PAD film as the absorber layer (hereafter referred to as "pristine" devices), while for the other type, we posttreated the PAD absorber layer via hot-pressing (referred to as "pressed" devices).

Figure 4a shows cross-section SEM images of the resulting n–i–p solar cell stacks with pristine (left) and pressed (right) MAPbI$_3$ film. To allow for a systematic comparison of the morphology before and after pressing, we choose devices with similar thickness. From Figure 4a, the glass substrate covered with ITO electrode (grey), the SnO$_2$ ETL (purple), the perovskite film (brown), the spiro-MeOTAD HTL (green), and the gold top electrode can be distinguished.

Exemplary current density–voltage (J–V) curves for each solar cell type are plotted in Figure 4b. Both, the pristine and the pressed devices exhibit a diode-like dark current characteristic (rectangles). Under AM1.5G illumination, the J–V curves measured in reverse direction (colored circles) exhibit photovoltaic behavior for both the pristine and the pressed devices. Considering the J–V curves measured in forward direction

(grey circles), both types of devices show a pronounced hysteresis.

The solar cell metrics determined from the reverse measurement direction for 12 devices each are shown in Figure 3c for the pristine (red) and pressed (blue) absorber layer. These metrics were measured after storing the devices in dry ambient conditions in the lab for 9 weeks, where the metrics were stable and even slightly improved compared to the metrics measured 24 h after the fabrication (see Figure S9, Table S1 and S2, Supporting Information, for comparison between metrics determined 24 h and 9 weeks after fabrication including forward direction, for the operational stability, see Figure S10, Supporting Information). The mean open-circuit voltage (V_{OC}) for the pristine absorber layer is (0.90 ± 0.11) V, while the pressed devices exhibit an increased mean V_{OC} of (0.95 ± 0.04) V. The mean short-circuit current density (J_{sc}) also increases upon pressing from (7.2 ± 3.1) mA cm^{-2} for the pristine devices to (7.6 ± 2.7) mA cm^{-2} for the pressed devices. Similarly, the fill factor (FF) yields mean values of (52 ± 9)% and (56 ± 6)% for the pristine and pressed absorber layers, respectively. Overall, the resulting average PCE for the pristine absorber layer of (3.5 ± 1.8)% improves to a PCE of (4.1 ± 1.8)% for the pressed absorber layer, where the champion devices of
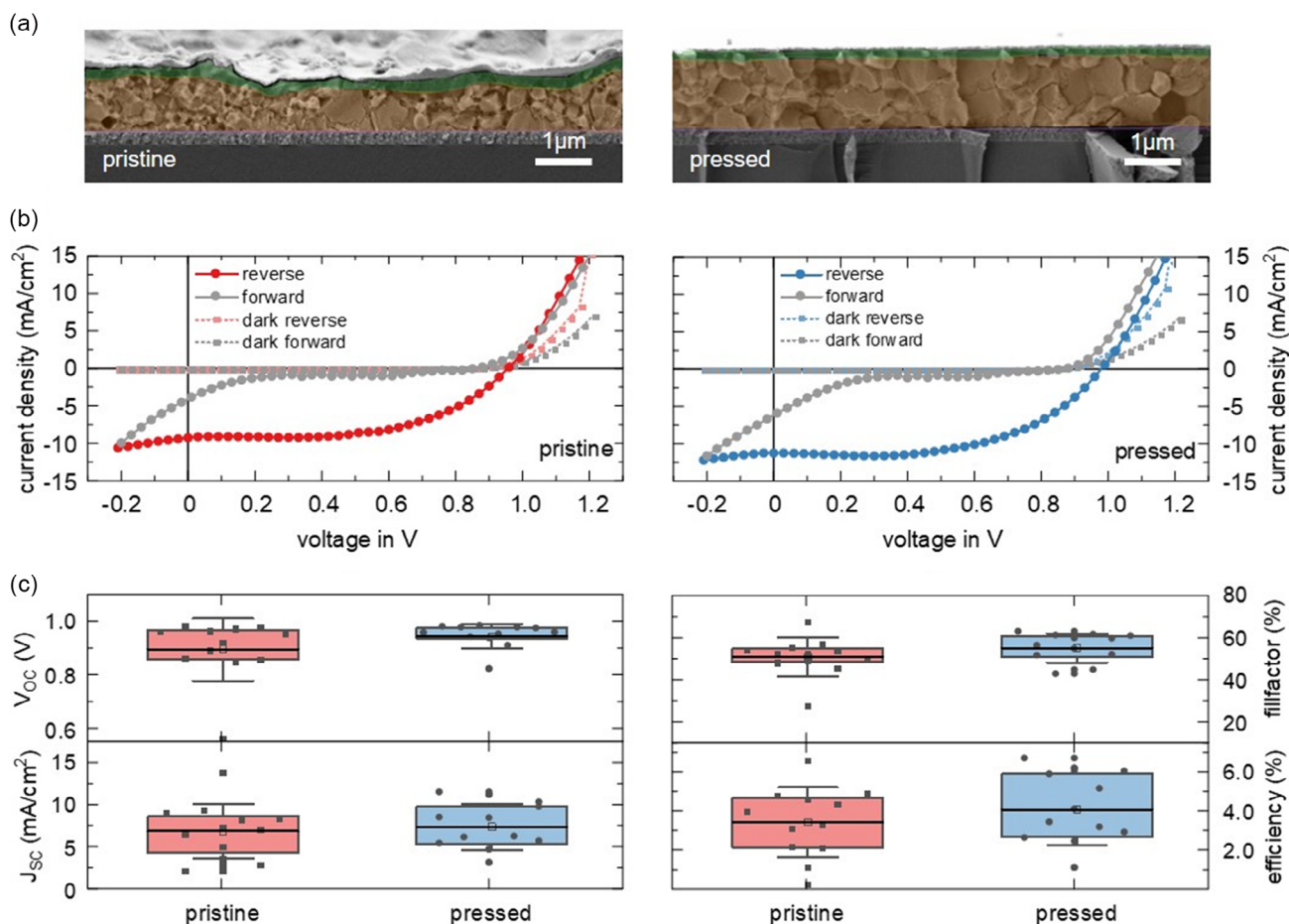

Figure 4. a) SEM cross-section images and b) current density–voltage (J–V) curves of a MAPbI$_3$ solar cell with a pristine (left) and with a pressed (right) PAD-processed absorber layer. c) Batch statistics (reverse direction) of solar cells fabricated with a pristine (red) and with a pressed (blue) absorber layer.

Table 1. Summary of solar cell metrics (mean values; individual champion values in brackets) for MAPbI$_3$ solar cells with pristine and with pressed PAD-processed absorber layer as extracted from reverse direction.

Type	V_{oc} [V]	J_{sc} [mA cm^{-2}]	FF [%]	PCE [%]
Pristine	0.90 ± 0.11 (0.96)	7.2 ± 3.1 (13.9)	52 ± 9 (49.5)	3.5 ± 1.8 (6.6)
Pressed	0.95 ± 0.04 (0.98)	7.6 ± 2.7 (11.2)	56 ± 6 (56.5)	4.1 ± 1.8 (6.2)

both types show an efficiency of >6% (see **Table 1** for a summary of the device metrics extracted from the reverse direction). Evidently, the additional pressing as posttreatment step results in a clearly increased number of devices with an efficiency of more than 6%.

Comparing these results with MAPbI$_3$ n–i–p solar cells that are solution-processed under ambient conditions with typical PCE values in the range of ≈15%,[49–53] it becomes clear that the V_{OC} values are in good agreement with literature values (0.85–1.10 V). While the FF values are at the lower end of the reported range (55%–75%), the obtained J_{sc} values are clearly below the literature values of around 21 mA cm^{-2}. Thus, the low J_{sc} values of our PAD-processed perovskite solar cells are the main limiting factor for the clearly lower PCE compared to corresponding solution-processed PSCs.

To better understand the origins of the losses and limitations in our PSCs with dry-processed MAPbI$_3$ film, in the following, we systematically investigate the device stack layer by layer, also deriving perspectives for strategies to optimize the PCE.

4. Detailed Evaluation of the Solar Cell Stack

4.1. SnO$_2$ Layer

First, we investigate the SnO$_2$ layer, acting as the ETL. To ensure proper electrical contact between the ETL and the MAPbI$_3$ film, sufficient physical contact and adhesion between both are mandatory. The physical contact is confirmed in the cross-section SEM image in **Figure 5**a. By scotch tape tests, we observe that the pristine MAPbI$_3$ film remains on the ETL after repeated applying and peeling off of a stripe of tape (Figure S11, Supporting Information), confirming good mechanical adhesion between ETL and perovskite film. On the peeled-off tape, only a marginal amount of MAPbI$_3$ powder is visible (Figure S11, Supporting Information), which stems from loose and uncompressed powder particles remaining on top of the film after PAD.

The ETL layer is subject to high mechanical and thermal stress during MAPbI$_3$ film deposition via PAD and pressing at elevated temperatures. During the deposition of the MAPbI$_3$ film via PAD, the accelerated perovskite powder particles impact on the ETL and potentially affect its electrical and optical properties. Similarly, the combination of pressure and temperature during hot-pressing may also alter the ETL properties.

To identify such potential changes in ETL properties, we carried out morphology characterizations and conductive atomic force microscopy (cAFM) for four different samples: 1) a native SnO$_2$ layer serving as reference, 2) a SnO$_2$ layer after removing a solution-processed MAPbI$_3$ film, 3) a SnO$_2$ layer after removing a pristine MAPbI$_3$ PAD film, and 4) a SnO$_2$ layer after removing a
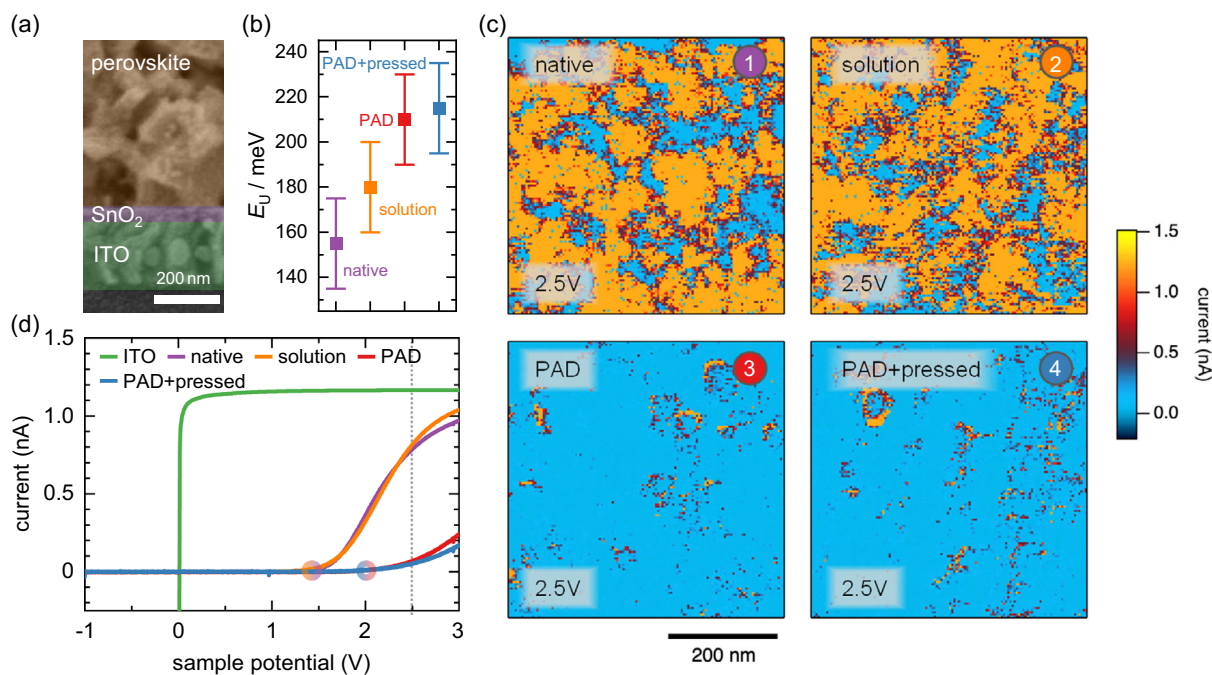

Figure 5. a) Cross-section SEM image of MAPbI$_3$ PAD film on indium tin oxide (ITO)/SnO$_2$. b) Urbach energy E_U of 1) a native SnO$_2$ layer serving as reference, 2) SnO$_2$ layer after removing a solution-processed MAPbI$_3$ film, 3) SnO$_2$ layer after removing a pristine MAPbI$_3$ PAD film, and 4) SnO$_2$ layer after removing a pressed MAPbI$_3$ PAD film. c) Conductive atomic force microscopy (cAFM) measurements at 2.5 V for the samples in (b). d) Current–voltage (I–V) characteristics for the samples in (c), averaged over the whole investigated area. For comparison, the I–V curve of an ITO layer is also shown.

pressed MAPbI$_3$ PAD film. The MAPbI$_3$ films were removed by dissolving them in dimethyl sulfoxide (DMSO).

First, we address possible changes in morphology and layer properties, where a reduction of the SnO$_2$ layer thickness or a fractioning of the grains within the layer might occur due to the PAD process. Here, height profiles of the four SnO$_2$ samples suggest that the SnO$_2$ layer thickness does not reduce due to the PAD process (see Figure S12, Supporting Information). Furthermore, no morphological changes between samples (1) and (4) are observed in atomic force microscopy (AFM) images (Figure S13, Supporting Information), suggesting that no lateral fractioning of the SnO$_2$ grains in the layer occurs.

In contrast to the morphology, the electrical properties of the ETL clearly change after the PAD deposition and pressing, as evident from cAFM measurements. At an applied potential of 2.5 V, the cAFM images (Figure 5c) show a decreased current for samples (3) and (4), compared to samples (1) and (2). This decreased current at 2.5 V is also reflected in corresponding I–V curves between −1 and 3 V (Figure 5d), where the current is averaged over the whole sampled areas in Figure 5c. Here, for samples (1) and (2), the onset potential is 1.4 V, compared to ≈2.0 V for samples (3) and (4), where also the steepness of the current rise appears lower compared to the corresponding steepness of samples (1) + (2). The latter observation suggests a lower electric conductivity in the ETLs that exhibited a prior PAD MAPbI$_3$ processing.

To better understand the origin of the decreased electrical conductivity of the PAD-treated SnO$_2$ layers, we conducted optical absorption measurements of all four SnO$_2$ samples in an integrating sphere, with a focus on investigating their Urbach absorption edge (Figure S14, Supporting Information). From the latter, we extract the so-called Urbach energy, a measure for the degree of energetic disorder within the investigated material.[54,55] Our analysis suggests that samples (3) + (4) exhibit E_U values in the range of ≈210 meV, compared to E_U values in the range of 160–180 meV for samples (1) + (2) (Figure 5b), indicating that indeed the PAD processing increases the energetic disorder and thus also the defect density of the SnO$_2$ ETL layer.

Here, increased disorder and defect density could result from the harsh impact of the MAPbI$_3$ powder particles and agglomerates on the SnO$_2$, where high mechanical stress might foster the formation of defects. Another aspect that could explain the increased disorder values for samples (3) + (4) is the incorporation of MAPbI$_3$ constituents into the SnO$_2$ layer. To investigate the latter aspect in more detail, we performed X-ray photoelectron spectroscopy (XPS) survey scans of all four samples, showing that lead species (signals at 138/143 and 414/436 eV) are present in samples (2)–(4) even after thorough removal of MAPbI$_3$ with DMSO (Figure S15, Supporting Information).[56,57] Here the Pb-concentration in samples (3) + (4) is ≈3–4 at%, twice as high as in sample (2). Interestingly, in all four samples we do not detect any iodine signals (619/631 eV).[56] This emphasizes that no iodoplumbate residuals are present on the SnO$_2$ layer, but rather metallic lead remains in the SnO$_2$ layer.

The incorporation of various materials such as Sb, Cr, or Nb$_2$O$_5$ into SnO$_2$ is known to lead to increased E_U (i.e., energetic disorder), and to a shift of the onset potential toward higher values,[58–60] fully in line with the findings from Figure 5. Thus, we conclude that the incorporation of Pb into the SnO$_2$

layers that exhibited a PAD-process contributes to the observed reduced conductivity and increased onset potential.

It is also clear that the increase in disorder is at first closely linked to the PAD process method. However, this issue could be addressed in the future, e.g., with the help of defect-chemical approaches, where, for example, Ru- or Sb-doped SnO$_2$ could be used to compensate for the presence of the Pb-induced defects.[61,62]

To counteract a possible mechanically induced increase in disorder, the use of SnO$_2$ layers with a more robust morphology and potentially higher mechanical hardness appears promising. For example, it was shown that SnO$_2$ layers prepared by an e-beam process show remarkably compact morphologies and that sputtered SnO$_2$ layers, in contrast to other preparation methods, show higher hardness values of up to 14 GPa.[63] Furthermore, it could be demonstrated that SnON coatings resulting from the incorporation of nitrogen into SnO$_2$ can exhibit hardness values of up to 23 GPa while maintaining excellent electrical properties.[64]

These examples underline that, by choosing a suitable preparation method and introducing additional constituents, it appears possible to produce mechanically more robust and defect-chemically optimized SnO$_2$ layers that still feature desired electrical properties even after the harsh mechanical treatment during perovskite powder deposition by PAD.

4.2. Dry-Processed MAPbI$_3$ Absorber Layer

Next, we investigate the film properties of our pristine and pressed MAPbI$_3$ thin films.

We first addressed whether our anti-sticking silanization coating (molecular formula: C$_{18}$H$_{37}$Cl$_3$Si) is transferred to our MAPbI$_3$ films upon pressing. **Figure 6**a shows an XPS spectrum of a pressed perovskite film, where only peaks corresponding to MAPbI$_3$ constituents and in particular no signatures of Si are visible.[56,65,66] Thus, we conclude that no significant amount of silane is transferred to the perovskite film during our pressing process.

Concerning the morphology of both types of MAPbI$_3$ films, deposited with our modified PAD setup, corresponding cross-section SEM images show that the pristine film is dense and void free, with a surface roughness in the range of Ra ≈ 200 nm (Figure 4a left). The films exhibit a thickness of about 1 μm. While the perovskite film thickness of highly efficient solar cells often is below 1 μm, it was shown that a PCE of 20% can be achieved using MAPbI$_3$ films with thickness of about 1 μm, if the grain size is large thus the number of grain boundaries in vertical direction is low.[67] Cross-sectional SEM images of the pressed film demonstrate that hot-pressing increases the grain size, narrows grain boundaries, reduces surface roughness, and diminishes the number of pores (Figure 4a, right), indicating morphology improvements toward better PCE. These morphology improvements are fully consistent with the insights gained in Section 2.2 and 2.3., and can be associated to stem from a sintering effect occurring during hot-pressing.[27,68] From XPS measurements in a previous work, it is known that hot-pressing induces small amount of PbI$_2$ at the MAPbI$_3$ film surface.[28] However, in Figure S18, Supporting Information, the XRD

ADVANCED
SCIENCE NEWS
www.advancedsciencenews.com
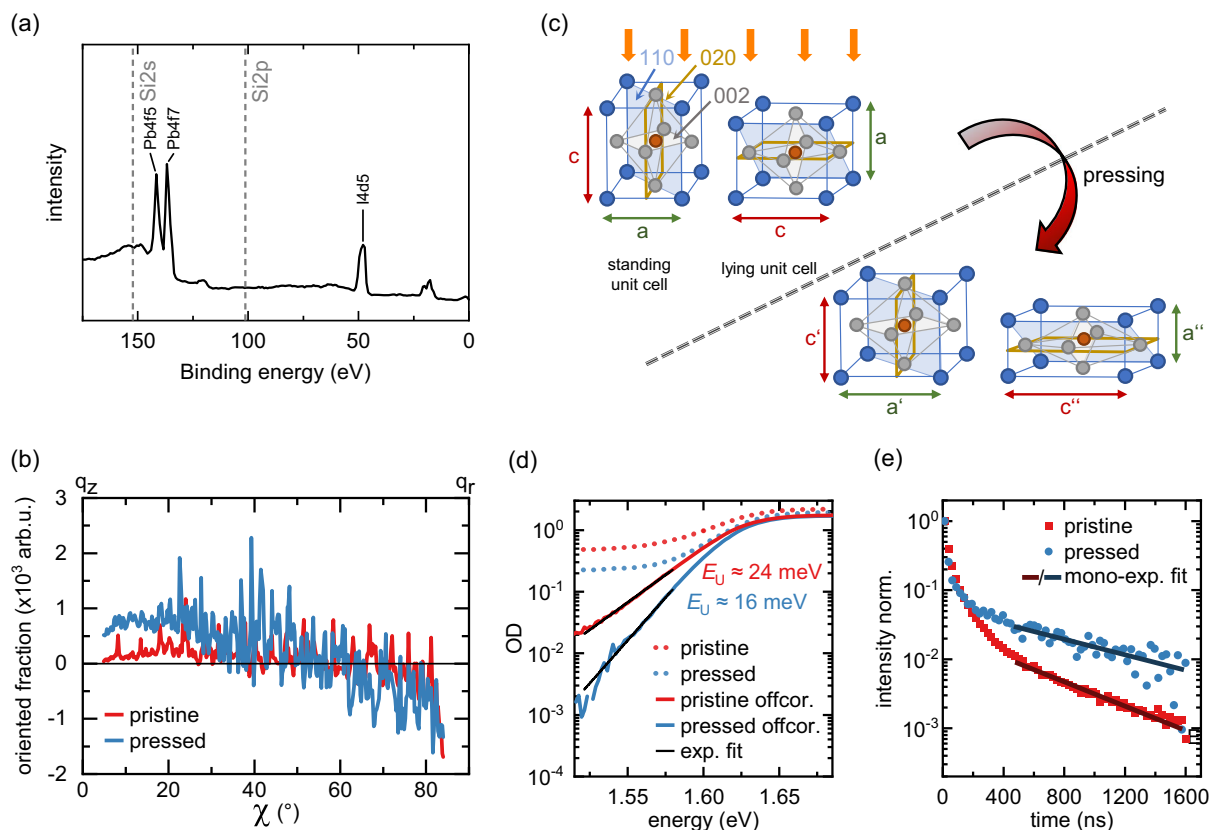
Solar
RRL
www.solar-rrl.com

Figure 6. a) XPS spectrum of a MAPbI₃ PAD film after pressing. b) Oriented fraction of the (110) and (002) double peak as a function of χ for a pristine (red) and pressed (blue) MAPbI₃ film determined by grazing incidence wide-angle X-ray scattering (GIWAXS). c) Sketch of unit cell deformation due to hot-pressing as indicated by GIWAXS. d) Absorption spectra of a pristine and pressed MAPbI₃ film on glass as measured (dotted) and offset corrected (line). The Urbach energy E_U is extracted from an exponential fit for each sample. e) Time-resolved photoluminescence of a pristine and pressed MAPbI₃ film on glass, together with a mono-exponential fit.

spectra show only a negligible amount of PbI₂ for the pressed film, that is, all MAPbI₃ films are considered to be essentially phase pure.

To characterize the crystallographic orientation of the pristine and pressed MAPbI₃ films, we performed grazing incidence wide-angle X-ray scattering (GIWAXS). The corresponding 2D GIWAXS patterns of a pristine and a pressed MAPbI₃ film (Figure S16, Supporting Information) were examined using a χ analysis, that is, a reciprocal space analysis as a function of direction, on the (110) & (002) double peak (Figure 6b). Therefore, a semicircular cut over the full peak width of the (110) & (002) double peak was extracted (details in Figure S16, Supporting Information). Hereby, 90° corresponds to the direction along q_r (in-plane of the sample) and 0° corresponds to the direction along q_z (out-of-plane of the sample). The intensity distribution along the χ arc of the pristine film (red line in Figure 6b) shows a random (isotropic) orientation of the crystallites. In contrast, the intensity along χ deviates from the isotropic distribution for the pressed film (blue line in Figure 6b), indicating a preferred orientation particularly in q_z-direction (planes parallel to sample surface) due to hot-pressing.

A single pixel analysis within the χ arc (details in Figure S16 and S17, Supporting Information) indicates an overall increased

number of large crystallites in the pressed film, consistent with XRD patterns measured in Bragg–Brentano geometry of pristine and pressed PAD-processed MAPbI₃ films (Figure S18, Supporting Information). Here, a smaller reflex width is found for a pressed film compared to a pristine film, again suggesting larger crystallite sizes in the pressed film. Moreover, the XRD patterns provide information about the crystallographic orientation in out-of-plane direction, where a random orientation is found in pristine films, changing to a (110) & (020)-preferred orientation upon pressing.

To further understand the impact of hot-pressing on the lattice parameters, we examine deformations of the unit cell by analyzing the GIWAXS data along different directions. The (110) and the (002) plane show the strongest changes as a function of direction. Depending on whether the interplanar distance d is examined parallel to the substrate (Figure S19 left, Supporting Information) or perpendicular to the substrate (Figure S19 right, Supporting Information), the separation increases or decreases upon hot-pressing. The shift of the (002) lattice spacing to smaller values along q_z in combination with the shift of the (110) spacing to larger values along q_r indicates the compression of the standing unit cell along the c-axis and its elongation along the a-axis (Figure 6c). Analogously, the change of the (002)

spacing to larger values along q_r, in combination with the shift of the (110) spacing to smaller values along q_z, indicates the compression of lying unit cells along the a-axis and their elongation along the c-axis (sketch in Figure 6c). Thus, the unit cells are flattened by pressing.

Overall, the analysis of the GIWAXS and XRD measurements suggest a compression of standing and lying MAPbI$_3$ unit cells, as well as an increase in (110)- and (020)-preferred orientation parallel to the substrate by hot-pressing. Such an increase in preferred orientation is known to correlate with improved excited-state properties.[28]

Thus, in the following, we analyze how the identified morphology differences between the pristine and pressed MAPbI$_3$ films are reflected in their optoelectronic properties. Figure 6d shows the optical absorption spectra of a pristine (red dotted line) and pressed (blue dotted line) MAPbI$_3$ film on glass with the typical absorption edge around 1.59 eV.[69,70] The absorption intensity for photon energies below the absorption edge is due to optical scattering, which we find to be strongly reduced for the pressed film compared to the pristine film. This indicates a more uniform morphology of the pressed film, in line with the previously identified higher compaction after hot-pressing. The Urbach energy, E_U, extracted from exponential fits to the offset corrected spectra, clearly reduces from (24.3 ± 0.2) meV for the pristine film to (15.5 ± 0.2) meV for the pressed film (see also Figure S20, Supporting Information), where the latter E_U value is in line with typical Urbach energies of solution-processed MAPbI$_3$ films.[55,71,72] The reduction of the Urbach energy upon pressing suggests less energetic disorder and a reduction in associated defect density in the pressed film.[73–75]

To examine differences in defect density between the PAD-processed films in more detail, we measured time-resolved photoluminescence (TRPL) decay curves after laser excitation (Figure 6e). Here, we considered pristine (red squares) and pressed (blue dots) MAPbI$_3$ films deposited on glass to exclude any impact of charge recombination processes at the perovskite/ETL interface. Compared to the pristine film, the pressed film shows a slower decrease of the TRPL intensity at times longer than 200 ns. By fitting the tail of the TRPL curves after 400 ns with a mono-exponential function (lines in Figure 6e), we extracted the defect-associated nonradiative decay rates k_1 according to

$$PL(t) \propto A_1 \times \exp(-2 \times k_1 \times t) \qquad (1)$$

By doing so, we find k_1 values of $(10.1 \pm 0.3) \times 10^5$ and $(6.5 \pm 0.6) \times 10^5 \, \text{s}^{-1}$ for the pristine and the pressed film, respectively. Thus, our films exhibit k_1 values similar to typical values of solution-processed MAPbI$_3$ films.[76,77] The decrease in defect-associated decay rate upon pressing transfers to an increase in charge-carrier lifetime from (493 ± 15) ns for the pristine film to (768 ± 66) ns for the pressed film, indicating less defects being present in pressed films.

Overall, our characterizations of the pristine and pressed PAD-processed MAPbI$_3$ films prove that they exhibit suitable morphology and optoelectronic properties for solar cell application, in particular when the films are posttreated by pressing.

4.3. Perovskite-Transport Layer Interfaces

Having verified the satisfactory optoelectronic and morphological properties of the PAD-processed MAPbI$_3$ films, we finally evaluate the interface between the perovskite film and both charge-transport layers (ETL and HTL).

By light-intensity-dependent J–V measurements and corresponding analysis of the solar cell metrics, Glowienka et al. in detail investigated the electrical functionality of the perovskite/ETL and perovskite/HTL interfaces. Together with drift-diffusion modeling, they succeeded in pinpointing the dominating performance limiting effects in their perovskite solar cells.[78]

Following this approach, we measured the J–V curves for the pristine (red triangles) and pressed (blue dots) PAD-processed MAPbI$_3$ solar cells. We then compared the light dependency of the measured solar cell metrics with the expectations from Glowienka et al. for an ideal (i.e., without any recombination processes) and a more realistic (i.e., including perovskite bulk and interface recombination) perovskite solar cell. **Figure 7**a shows the experimentally determined light-intensity-dependent FF and V_{oc} of our devices, while in Figure 7b, the corresponding expectations from Glowienka et al. are shown.

For our devices with pristine and pressed absorber layer, the FF increases in the light intensity range from 10^{-3} to 10^{-1} sun. In contrast to the devices with pressed MAPbI$_3$ film where the FF monotonously increases, the FF of the devices with pristine MAPbI$_3$ film decreases again for light intensities above 10^{-1} sun. Overall, the pristine devices exhibit lower FF values over the whole measurement range. For an ideal device, the FF is expected to be independent of the light intensity, while including interface recombination, the FF is expected to exhibit a maximum. Furthermore, the presence of perovskite bulk recombination lowers the FF.[78] Comparing our experimental results with the theoretical expectations, it thus becomes clear that the light dependence of the FF in our case fits best to the theoretical expectations including interface recombination. Therefore, we conclude that in our PAD-processed solar cells interface recombination processes are present, limiting the overall device efficiency. Furthermore, the decrease of the FF for pristine devices above 10^{-1} sun indicates an increased interface recombination compared to pressed devices.[78] Furthermore, the overall lower FF values of the pristine devices compared to the pressed devices suggest more nonradiative recombination in the perovskite bulk of the pristine absorber layers, consistent with the higher nonradiative recombination rate k_1 found in the transient PL measurements (Figure 6e).

The V_{oc} for ideal device is expected to show a linear dependence on the light intensity in a semilogarithmic plot and a deviation at high intensities when interface recombination is present. For our pristine devices, we observe this deviation from the linear dependence for light intensities above 10^{-1} sun, further supporting that more pronounced interface recombination is present in the pristine devices than in the pressed devices.

To identify if monomolecular (trap-assisted, nonradiative) or bimolecular (band to band, radiative) recombination predominantly takes place at the interfaces, we determined the ideality factor n and the inverse Langevin recombination factor α from
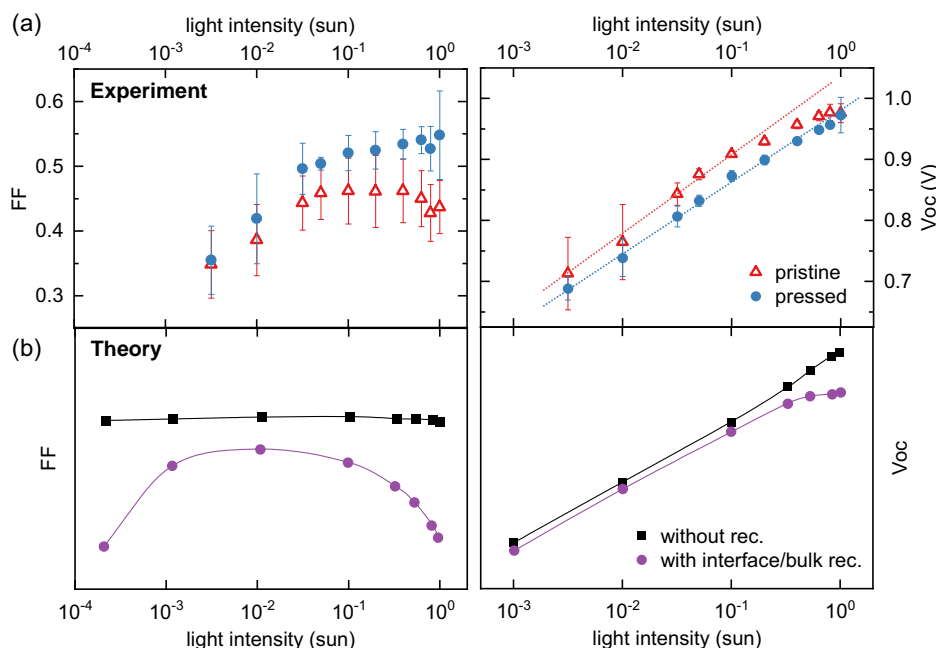
Figure 7. a) Measured light-intensity dependence of the fill factor (FF) (left) and the open-circuit voltage (V_{oc}) (right) for pristine (red triangles) and pressed (blue dots) MAPbI$_3$ absorber layers. b) Theoretical expectations for FF (left) and the V_{oc} (right) of ideal devices without any recombination (black squares) and of devices with recombination (purple circles), after Glowienka et al.[78] The lines in (a,b) serve as guide for the eye.

the V_{oc} versus J_{sc} plot and the J_{sc} versus light intensity plot, respectively (Figure S21, Supporting Information). In general, the ideality factor n ranges between values of 1 and 2, where a value of 1 is expected for ideal solar cells in which only bulk recombination occurs.[79] Deviations from 1 indicate energy misalignment and trap-assisted recombination at the interfaces.[80,81] We find values of $n \approx 2$ for all measured cells, which suggests trap-assisted monomolecular recombination as the dominant recombination mechanism at the interfaces in our case.

Theoretically expected values for α range from 0.5 to 1, with a value of 0.5 indicating pure bimolecular recombination and values close to 1 suggesting monomolecular recombination as the dominant recombination process. Thus, the extracted α values of ≈0.9 for our solar cells further support trap-assisted recombination being the dominant recombination mechanism at the interface.[82,83] This is consistent with the observed hysteresis in the J–V curves (Figure 4b) indicating an accumulation of ions at the interface, screening the internal electric field and promoting recombination there.[84]

Summing up the light-intensity-dependent investigations of the PAD-processed solar cells, we conclude that recombination losses at the interfaces between perovskite and charge-carrier extraction layers are present in our devices, likely contributing to their limited PCE. On the basis of our analyses, it is not possible to distinguish which interface (i.e., whether the perovskite/ETL or the perovskite/HTL interface) is predominantly responsible for the recombination losses. However, due to the alteration of the SnO$_2$ layer upon perovskite deposition via PAD discussed in Section 4.1, it is conceivable that the identified interface recombination losses mainly originate from the ETL/perovskite interface.

However, another aspect that might contribute to significant interface recombination and thus limit current values in our devices is the presence of hydrates at the transport layer/perovskite interface. The processing of the ETL and the perovskite, including pressing, was carried out under ambient conditions (relative humidity: 40%–50%), that is, within a humidity range, where the formation of monohydrates at the perovskite surface is known to happen.[85] And indeed the formation of hydrates on the perovskite film in our case can already be conjectured from the grey tarnishing perovskite surface after PAD processing (Figure 3b). It was shown that hydrates are mainly formed at the surface and the grain boundaries of the perovskite, where they act as defects within the perovskite film and the interface.[85,86] Thus, the presence of hydrates lead to additional pathways for charge recombination, reducing charge extraction from the perovskite to the transport layer. This is in line with the generally low current density of our PAD-processed devices.[87,88] Furthermore, the presence of hydrates also reduces the barrier for ion migration,[89] facilitating hysteresis in J–V curves of corresponding PSCs,[90] which is also fully consistent with our results in Section 3. Thus, we presume that the presence of hydrates also contributes considerably to the limited performance and pronounced hysteresis of the PAD-processed solar cells.

5. Conclusion and Perspective

We have successfully manufactured the first solar cells containing a completely dry-processed powder-based MAPbI$_3$ absorber layer. These absorber layers were deposited via PAD, where necessary key modifications such as the use of an ejector and an

inertial separator unit were introduced into our setup, resulting in dense and void-free MAPbI₃ films with thicknesses of ≈1 μm.

The solar cells are fully working with champion device efficiencies >6% in backward direction. Here, the V_{oc} (0.95 V) values, and to some extent also the FF values (56%) match literature values of cells processed from solution under ambient conditions. However, in addition to a pronounced hysteresis between the J–V sweep directions, especially the low J_{sc} values (7.6 mA cm⁻²) limit the overall efficiency of our powder-processed devices.

We systematically analyzed our solar cell stacks and found that the pristine MAPbI₃ films show well-suited morphology and optoelectronic properties for solar cell application. The film properties further improve by posttreatment via (hot-)pressing, leading to increased grain size, crystallinity, crystallographic orientation, compaction, reduced surface roughness, and energetic disorder, as well as a longer charge-carrier lifetime, making the optoelectronic functionality of the optimized PAD-processed MAPbI₃ films to be on par with their typical solution-processed counterparts.

While the harsh mechanical impact of the MAPbI₃ powder particles in the course of the PAD process appears to not alter the SnO₂ layer thickness and its morphology, cAFM characterizations show a clearly reduced electrical functionality, that is, an increase of the onset potential for electrical conduction and a decreased overall conductivity. Here, absorption measurements indicate that the PAD processing increases the disorder of the SnO₂ layer. This increase could be associated to an increase in defect density within the SnO₂ due to the high mechanical impact, and/or the incorporation of metallic Pb into the SnO₂ (as suggested by XPS investigations).

Furthermore, analyzing light-intensity-dependent J–V measurements, we find that recombination at the interfaces between the perovskite and charge-transport layers also contributes to the limited performance of the PAD-processed solar cells.

Here, it appears plausible that the formation of hydrates at the perovskite surfaces, which lowers the barrier for ion migration associated to a more pronounced hysteresis, is a major contributing aspect, since the perovskite processing and posttreatment of our films happen under ambient conditions.

In summary, our work successfully demonstrates that it is possible to produce PSCs with completely dry-processed absorber layer based on perovskite powders. As we could pinpoint the main performance-limiting aspects to be associated with the presence of hydrates at the perovskite surface and the deterioration of the electrical properties of the SnO₂ layer due to the PAD process, optimized preparation methods and defect engineering of the SnO₂ layer, as well as moving all processing steps into a dry atmosphere and using passivated powders, represent important optimization strategies to reduce hysteresis and to improve overall device performance. Based on the various approaches already presented in the literature, we are thus confident that the current hurdles to optimize the efficiency of PAD-processed perovskite solar cells will be successfully overcome in the future.

6. Experimental Section

Powder Synthesis: For the mechanochemical synthesis of MAPbI₃, 1.9 g of the methylammonium iodide (MAI) reactant powder and 5.509 g of PbI₂

(99%, Acros Organics) were added to 80 mL ZrO₂ milling jars under ambient conditions. Then, 8 mL cyclohexane as a milling agent and 25 ZrO₂ milling balls with a diameter of 10 mm were added to the milling jar. A Fritsch "Pulverisette 5" planetary ball mill with 400 rpm was used for synthesis. After 5 min of milling, a pause of 20 min was implemented to prevent excessive heating of the milling jar. The process was repeated until a total milling time of 50 min was achieved. Afterward, the cyclohexane was evaporated in air and the obtained black MAPbI₃ powder was sieved using a mesh size of 63 μm.

Solar Cell Fabrication: Substrate Preparation and ETL: Substrates were cleaned in an ultrasonic bath with soap water (Hellmanex), deionized water, acetone, and isopropanol and treated with UV–ozone. SnO₂ nanoparticles (Alfa Aesar 15% in H₂O) were spin-coated onto the clean substrate at 3000 rpm for 30 s and the substrates were annealed at 180 °C for 30 min and again UV–ozone treated prior to perovskite deposition.

Solar Cell Fabrication: Perovskite Film Deposition: MAPbI₃ films were produced via PAD method using a custom-made apparatus. Prior to deposition, the mechanochemically synthesized MAPbI₃ powder was dried for at least 1 h at 120 °C. For each film, 1 g of the dried powder was filled into the aerosol generation unit. Using helium as a processing gas, 0.25 L min⁻¹ were passed through the unit to generate the aerosol while the ejector was fed with 20 L min⁻¹ to enhance acceleration of the aerosol through the converging slit nozzle with orifice size of 10 × 0.5 mm. The substrate to nozzle distance was set to 3 mm. The substrate was moved past the nozzle 30 times at a velocity of 1 mm s⁻¹. During deposition, a pressure of 122 mbar resulted in the aerosol generation unit and 6 mbar in the deposition chamber (for details about chosen PAD process parameters, as well as a discussion about lead safety considerations for the PAD, see Section S1, Supporting Information). The MAPbI₃ films for untreated devices were blown off with nitrogen before the HTL layer was applied to remove the loose MAPbI₃ particles on the surface.

Solar Cell Fabrication: HTL and Back Contact: Spiro-MeOTAD (Sigma Aldrich) solutions (72.5 mg mL⁻¹ in chlorobenzene (CB), 17.5 mL Li-TFSI [520 mg mL⁻¹ in acetonitrile], 42.5 mL tBP) were spin-coated at 3000 rpm for 30 s onto the perovskite film. Finally, 100 nm gold was thermally evaporated onto the substrates as back contact which results in active area of 12.5 mm² for each solar cell.

Solar Cell Fabrication: Pressing: Pristine MAPbI₃ PAD films were hot-pressed with a homebuilt manual press (details on press setup in previous work).[28] The films were pressed with 25 MPa at 120 °C for 5 min (at target levels). For optimum pressing results, loose powder particles and agglomerates on the pristine PAD films were removed by means of a nitrogen gun before the pressing process. The glass blocks used as press die were treated with an anti-sticking coating (trichloro(octadecyl)silane in toluene from liquid phase) to prevent the pressed film from sticking.

Solar Cell Characterization: The J–V curves were obtained using an ORIEL Sol2A (Newport) solar simulator with a calibrated AM 1.5 G spectrum in combination with a Keithley 2400 sourcemeter and an aperture mask of 10 mm². The scan rate for all measurements was set to 150 mV s⁻¹. For the light-intensity-dependent measurements different neutral density filters were placed above the devices to reduce the light intensity.

Absorption: Absorption spectra were recorded using a Cary 5000 (Varian) equipped with an integrating sphere in reflection mode.

TRPL: For TRPL curves, time-correlated single-photon counting (TCSPC) measurements were performed with a PicoQuant MT200 confocal fluorescence microscope in combination with a PMA Hybrid PMT 40 photomultiplier tube (PicoQuant) and a TimeHarp 260 Pico TCSPC board (PicoQuant). The samples were excited with a 560 nm diode Laser (PicoQuant LDH-D-TA-560) with a frequency of 2.0 MHz and a pulse width of 68 ps. The laser beam was focused on the sample with an Olympus Objective with 4× magnification and the emission was filtered with a 561 nm long-pass filter before detection. The excitation fluence was set to 300 nJ cm⁻².

AFM: AFM was performed using a dimension ICON-GB system, equipped with a Nanoscope V controller (Bruker Corp., USA). The AFM unit was located in a glove box under argon atmosphere (water < 5 ppm; oxygen < 0.1 ppm). Multidimensional IV-Spectroscopy images were

obtained using the DataCube-TUNA mode of the measurement system in combination with the PF-TUNA application module. We used a conductive NSC14/Cr-Au Probe from MikroMasch for nanoscale electrical characterization (calibrated spring constant via Sader: 6.9 N m^{-1}). The applied loading force for I–V measurements was 100 nN and the sample bias voltage was swept from −1 to 3 V. The maximum current was limited to ±1.3 nA. Data processing and visualization of multidimensional AFM data was performed using Igor Pro (Wavemetrics Inc., USA). Additional AFM topography images (Supporting Information) were recorded under ambient conditions in TappingMode, using an AC160TS-R3 probe (Olympus Corp., Japan) with a nominal resonance frequency of 300 kHz.

GIWAXS: GIWAXS experiments were conducted at the beamline 7.3.3 at the Advanced Light Source at Lawrence Berkeley National Lab (Berkeley, USA).[91] The samples were illuminated with 10 keV radiation ($\lambda = 1.24$ Å) at an incident angle (α_i) of 0.25° at room temperature. The beam size was 300 μm (height) × 700 μm (width). The scattering signal was captured on a Pilatus 2M (172 μm pixel size, file format EDF, 1475 × 1679 pixels) located 274 mm from the sample. Acquisition times were 10 s for each frame. After correction for Ewald-sphere curvature with Xi-CAM,[92] the 2D data was reduced to 1D horizontal and vertical cuts using customized Python scripts. The software DPDAK (v1.4.1)[93] was used for Chi-integration. To track scattering peak parameters, the 1D intensity profiles were fitted with Gaussians and a local background using a Trust-Region-Reflective Least Squares algorithm.

X-Ray Diffraction: A Bruker "D8 Discover A25" with Cu-K$_{\alpha l}$ radiation ($\lambda = 0.15406$ nm) and Ge-K$_{\alpha l}$ monochromator in reflection mode was used to acquire XRD patterns with a 2θ step size of 0.008° in the 2θ range from 10° to 45° under ambient conditions. The X-ray source was operated with 40 kV and 40 mA.

Film Thickness and Surface Roughness: The film thickness and surface roughness Ra of the (pressed) PAD films were measured using either an LSM 900 M (Carl Zeiss AG) laser scanning microscope with a 405 nm laser or using a profilometer (Dektak 150, Veeco).

SEM: The film morphology was characterized by SEM using a Zeiss Leo 1530 instrument FE-SEM with Schottky-field-emission cathode, In-lens detector, and SE2 detector. The accelerating voltage was 3 kV. Prior to measurement, the samples were sputtered with 2 nm platinum.

XPS: XPS measurements were carried out with a Versa Probe III photoelectron spectrometer (PHI). The excitation was provided by an Al K α source ($h\nu = 1486.6$ eV) at a pass energy of 224 eV to achieve high sensitivity. The X-ray beam had a diameter of 100 μm and a power of 25 W. Ion (Ar$^+$) and electron neutralization was applied to the sample to avoid charging-induced energy shifts.

Supporting Information

Supporting Information is available from the Wiley Online Library or from the author.

Acknowledgements

Conflict of Interest

The authors declare no conflict of interest.

Data Availability Statement

The data that support the findings of this study are available from the corresponding author upon reasonable request.

Keywords

[1] NREL, Best Research-Cell Efficiency Chart **2023**, https://www.nrel.gov/pv/cell-efficiency.html (accessed: April 2023).

[2] J. Jeong, M. Kim, J. Seo, H. Lu, P. Ahlawat, A. Mishra, Y. Yang, M. A. Hope, F. T. Eickemeyer, M. Kim, Y. J. Yoon, I. W. Choi, B. P. Darwich, S. J. Choi, Y. Jo, J. H. Lee, B. Walker, S. M. Zakeeruddin, L. Emsley, U. Rothlisberger, A. Hagfeldt, D. S. Kim, M. Grätzel, J. Y. Kim, *Nature* **2021**, *592*, 381.

[3] Q. Cao, Y. Li, H. Zhang, J. Yang, J. Han, T. Xu, S. Wang, Z. Wang, B. Gao, J. Zhao, X. Li, X. Ma, S. M. Zakeeruddin, W. E. I. Sha, X. Li, M. Grätzel, *Sci. Adv.* **2021**, *7*, eabg0633.

[4] Y. Zhao, T. Heumueller, J. Zhang, J. Luo, O. Kasian, S. Langner, C. Kupfer, B. Liu, Y. Zhong, J. Elia, A. Osvet, J. Wu, C. Liu, Z. Wan, C. Jia, N. Li, J. Hauch, C. J. Brabec, *Nat. Energy* **2022**, *7*, 144.

[5] H. Li, J. Zhou, L. Tan, M. Li, C. Jiang, S. Wang, X. Zhao, Y. Liu, Y. Zhang, Y. Ye, W. Tress, C. Yi, *Sci. Adv.* **2022**, *8*, eabo7422.

[6] J. Li, H. Wang, X. Y. Chin, H. A. Dewi, K. Vergeer, T. W. Goh, J. W. M. Lim, J. H. Lew, K. P. Loh, C. Soci, T. C. Sum, H. J. Bolink, N. Mathews, S. Mhaisalkar, A. Bruno, *Joule* **2020**, *4*, 1035.

[7] S. Biberger, K. Schötz, P. Ramming, N. Leupold, R. Moos, A. Köhler, H. Grüninger, F. Panzer, *J. Mater. Chem. A* **2022**, *10*, 18038.

[8] K. Schötz, C. Greve, A. Langen, H. Gorter, I. Dogan, Y. Galagan, A. J. J. M. van Breemen, G. H. Gelinck, E. M. Herzig, F. Panzer, *Adv. Opt. Mater.* **2021**, *9*, 2101161.

[9] O. Telschow, M. Albaladejo-Siguan, L. Merten, A. D. Taylor, K. P. Goetz, T. Schramm, O. V. Konovalov, M. Jankowski, A. Hinderhofer, F. Paulus, F. Schreiber, Y. Vaynzof, *J. Mater. Chem. A* **2022**, *10*, 19743.

[10] K. P. Goetz, Y. Vaynzof, *ACS Energy Lett.* **2022**, *7*, 1750.

[11] W. Massmann, *Occup. Environ. Med.* **1956**, *13*, 51.

[12] G. L. Kennedy, *Drug Chem. Toxicol.* **1986**, *9*, 147.

[13] D. Liu, C. J. Traverse, P. Chen, M. Elinski, C. Yang, L. Wang, M. Young, R. R. Lunt, *Adv. Sci.* **2018**, *5*, 1700484.

[14] X. Cao, G. Zhang, Y. Cai, L. Jiang, X. He, Q. Zeng, J. Wei, Y. Jia, G. Xing, W. Huang, *Sol. RRL* **2020**, *4*, 2000008.

[15] S. Öz, J. Burschka, E. Jung, R. Bhattacharjee, T. Fischer, A. Mettenbörger, H. Wang, S. Mathur, *Nano Energy* **2018**, *51*, 632.

[16] H.-S. Kim, Y.-J. An, J. I. Kwak, H. J. Kim, H. S. Jung, N.-G. Park, *ACS Energy Lett.* **2022**, *7*, 1154.

[17] A. These, N. H. Khansur, O. Almora, L. Luer, G. J. Matt, U. Eckstein, A. Barabash, A. Osvet, K. G. Webber, C. J. Brabec, *Adv. Electron. Mater.* **2021**, *7*, 2001165.

[18] M.-Y. Cho, S. Kim, I.-S. Kim, E.-S. Kim, Z.-J. Wang, N.-Y. Kim, S.-W. Kim, J.-M. Oh, *Adv. Funct. Mater.* **2020**, *30*, 1907449.

[19] N. Leupold, A. L. Seibel, R. Moos, F. Panzer, *Eur. J. Inorg. Chem.* **2021**, *2021*, 2882.

[20] K. Naoe, M. Nishiki, A. Yumoto, *J. Therm. Spray Technol.* **2013**, *22*, 1267.

[21] H. S. Ryu, T. S. Lim, J. Ryu, S.-H. Hong, *J. Electrochem. Soc.* **2012**, *160*, C42.

[22] J.-Y. Park, K.-A. Lee, S.-H. Kim, G.-S. Ham, *Arch. Metall. Mater.* **2017**, *62*, 2017.

[23] J.-H. Park, D.-S. Park, B.-D. Hahn, J.-J. Choi, J. Ryu, S.-Y. Choi, J. Kim, W.-H. Yoon, C. Park, *Ceram. Int.* **2016**, *42*, 3584.

[24] M. Schubert, D. Hanft, T. Nazarenus, J. Exner, M. Schubert, P. Nieke, P. Glosse, N. Leupold, J. Kita, R. Moos, *Funct. Mater. Lett.* **2019**, *12*, 1930005.

[25] J. Akedo, *J. Ceram. Soc. Jpn.* **2020**, *128*, 101.

[26] F. Panzer, D. Hanft, T. P. Gujar, F.-J. Kahle, M. Thelakkat, A. Köhler, R. Moos, *Materials* **2016**, *9*, 277.

[27] C. Witt, A. Schmid, N. Leupold, M. Schultz, J. Höcker, A. Baumann, R. Moos, F. Panzer, *ACS Appl. Electron. Mater.* **2020**, *2*, 2619.

[28] C. Witt, K. Schötz, M. Kuhn, N. Leupold, S. Biberger, P. Ramming, F.-J. Kahle, A. Köhler, R. Moos, E. M. Herzig, F. Panzer, *J. Phys. Chem. C* **2023**, *127*, 10563.

[29] P. Ramming, N. Leupold, K. Schötz, A. Köhler, R. Moos, H. Grüninger, F. Panzer, *J. Mater. Chem. C* **2021**, *9*, 11827.

[30] S. Shrestha, R. Fischer, G. J. Matt, P. Feldner, T. Michel, A. Osvet, I. Levchuk, B. Merle, S. Golkar, H. Chen, S. F. Tedde, O. Schmidt, R. Hock, M. Rührig, M. Göken, W. Heiss, G. Anton, C. J. Brabec, *Nat. Photonics* **2017**, *11*, 436.

[31] W. A. Dunlap-Shohl, T. Li, D. B. Mitzi, *ACS Appl. Energy Mater.* **2019**, *2*, 5083.

[32] W. Kim, M. S. Jung, S. Lee, Y. J. Choi, J. K. Kim, S. U. Chai, W. Kim, D.-G. Choi, H. Ahn, J. H. Cho, D. Choi, H. Shin, D. Kim, J. H. Park, *Adv. Energy Mater.* **2018**, *8*, 1702369.

[33] A. Mayer, M. Buchmüller, S. Wang, C. Steinberg, M. Papenheim, H.-C. Scheer, N. Pourdavoud, T. Haeger, T. Riedl, *J. Vac. Sci. Technol. B* **2017**, *35*, 06G803.

[34] J. Xiao, Y. Yang, X. Xu, J. Shi, L. Zhu, S. Lv, H. Wu, Y. Luo, D. Li, Q. Meng, *J. Mater. Chem. A* **2015**, *3*, 5289.

[35] N. Leupold, K. Schötz, S. Cacovich, I. Bauer, M. Schultz, M. Daubinger, L. Kaiser, A. Rebai, J. Rousset, A. Köhler, P. Schulz, R. Moos, F. Panzer, *ACS Appl. Mater. Interfaces* **2019**, *11*, 30259.

[36] N. Leupold, P. Ramming, I. Bauer, C. Witt, J. Jungklaus, R. Moos, H. Grüninger, F. Panzer, *Eur. J. Inorg. Chem.* **2023**, *26*.

[37] J. Akedo, *J. Therm. Spray Technol.* **2008**, *17*, 181.

[38] D. Hanft, J. Exner, M. Schubert, T. Stöcker, P. Fuierer, R. Moos, *J. Ceram. Sci. Tech.* **2015**, *6*, 147.

[39] F. S. Kong, Y. Z. Jin, H. D. Kim, *Shock Waves* **2016**, *26*, 771.

[40] B. A. Nejand, S. Gharibzadeh, V. Ahmadi, H. R. Shahverdi, *Sci. Rep.* **2016**, *6*, 33649.

[41] L. Huang, Z. Xing, X. Tang, D. Li, X. Meng, X. Hu, T. Hu, Y. Chen, *J. Mater. Chem. A* **2021**, *9*, 16178.

[42] Y. Yu, M. Shang, T. Wang, Q. Zhou, Y. Hao, Z. Pang, D. Cui, G. Lian, X. Zhang, S. Han, *J. Mater. Chem. C* **2021**, *9*, 15056.

[43] A. Mayer, N. Pourdavoud, Z. Doukkali, K. Brinkmann, J. Rond, J. Staabs, A.-C. Swertz, P. van gen Hassend, P. Görrn, T. Riedl, H.-C. Scheer, *Appl. Phys. A* **2021**, *127*, 237.

[44] J. Moon, S. Kwon, M. Alahbakhshi, Y. Lee, K. Cho, A. Zakhidov, M. J. Kim, Q. Gu, *ACS Appl. Mater. Interfaces* **2021**, *13*, 5368.

[45] T. Zhang, L. Zhang, G. Zhu, Q. Cui, Q. Wang, G. Lian, Z. Zheng, H. Yu, *Adv. Mater. Interfaces* **2022**, *9*, 2200447.

[46] C. Qu, J. Hu, X. Liu, Z. Li, Y. Ding, *Materials* **2017**, *10*, 1329.

[47] T. Li, A. M. Zeidell, G. Findik, W. A. Dunlap-Shohl, J. Euvrard, K. Gundogdu, O. D. Jurchescu, D. B. Mitzi, *Chem. Mater.* **2019**, *31*, 4267.

[48] H. Chen, F. Ye, W. Tang, J. He, M. Yin, Y. Wang, F. Xie, E. Bi, X. Yang, M. Grätzel, L. Han, *Nature* **2017**, *550*, 92.

[49] G. Jang, H.-C. Kwon, S. Ma, S.-C. Yun, H. Yang, J. Moon, *Adv. Energy Mater.* **2019**, *9*, 1901719.

[50] R. Herckens, W. T. M. V. Gompel, W. Song, M. C. Gélvez-Rueda, A. Maufort, B. Ruttens, J. D'Haen, F. C. Grozema, T. Aernouts, L. Lutsen, D. Vanderzande, *J. Mater. Chem. A* **2018**, *6*, 22899.

[51] J. Su, H. Cai, X. Ye, X. Zhou, J. Yang, D. Wang, J. Ni, J. Li, J. Zhang, *ACS Appl. Mater. Interfaces* **2019**, *11*, 10689.

[52] C. Du, S. Wang, X. Miao, W. Sun, Y. Zhu, C. Wang, R. Ma, *Beilstein J. Nanotechnol.* **2019**, *10*, 2374.

[53] Z. Guo, L. Gao, Z. Xu, S. Teo, C. Zhang, Y. Kamata, S. Hayase, T. Ma, *Small* **2018**, *14*, 1802738.

[54] G. D. Cody, T. Tiedje, B. Abeles, B. Brooks, Y. Goldstein, *Phys. Rev. Lett.* **1981**, *47*, 1480.

[55] M. Ledinsky, T. Schönfeldová, J. Holovský, E. Aydin, Z. Hájková, L. Landová, N. Neyková, A. Fejfar, S. De Wolf, *J. Phys. Chem. Lett.* **2019**, *10*, 1368.

[56] J. Rodriguez-Pereira, J. Tirado, A. F. Gualdrón-Reyes, F. Jaramillo, R. Ospina, *Surf. Sci. Spectra* **2020**, *27*, 024003.

[57] M. J. Bozack, K. W. Bryant, *Surf. Sci. Spectra* **1992**, *1*, 324.

[58] S. B. O. dos Santos, M. H. Boratto, R. A. Ramos, L. V. A. Scalvi, *Mater. Chem. Phys.* **2022**, *278*, 125571.

[59] S. Tominc, A. Rečnik, Z. Samardžija, G. Dražić, M. Podlogar, S. Bernik, N. Daneu, *Ceram. Int.* **2018**, *44*, 1603.

[60] H. Zhao, W. Liang, F. Wang, Y. Zhou, Q. Xie, *Results Phys.* **2020**, *18*, 103314.

[61] Y. Bai, Y. Fang, Y. Deng, Q. Wang, J. Zhao, X. Zheng, Y. Zhang, J. Huang, *ChemSusChem* **2016**, *9*, 2686.

[62] S. Akin, *ACS Appl. Mater. Interfaces* **2019**, *11*, 39998.

[63] J. Chen, S. J. Bull, *J. Phys. Appl. Phys.* **2008**, *41*, 074009.

[64] H. J. Gwon, N.-R. Kang, Y. Lee, S. O. Won, H. J. Chang, J.-W. Choi, C.-Y. Kang, S. K. Kim, B. Kwon, S. Nahm, J.-Y. Kim, J.-S. Kim, S.-H. Baek, *Chem. Mater.* **2016**, *28*, 7051.

[65] G. M. Ingo, N. Zacchetti, D. della Sala, C. Coluzza, *J. Vac. Sci. Technol. Vac. Surf. Films* **1989**, *7*, 3048.

[66] A. Mesarwi, A. Ignatiev, *Surf. Sci.* **1991**, *244*, 15.

[67] Z. Liu, L. Qiu, E. J. Juarez-Perez, Z. Hawash, T. Kim, Y. Jiang, Z. Wu, S. R. Raga, L. K. Ono, S. (Frank) Liu, Y. Qi, *Nat. Commun.* **2018**, *9*, 3880.

[68] S. Deumel, A. van Breemen, G. Gelinck, B. Peeters, J. Maas, R. Verbeek, S. Shanmugam, H. Akkerman, E. Meulenkamp, J. E. Huerdler, M. Acharya, M. García-Batlle, O. Almora, A. Guerrero, G. Garcia-Belmonte, W. Heiss, O. Schmidt, S. F. Tedde, *Nat. Electron.* **2021**, *4*, 681.

[69] F. Panzer, C. Li, T. Meier, A. Köhler, S. Huettner, *Adv. Energy Mater.* **2017**, *7*, 1700286.

[70] K. P. Goetz, A. D. Taylor, F. Paulus, Y. Vaynzof, *Adv. Funct. Mater.* **2020**, *30*, 1910004.

[71] E. Ugur, M. Ledinský, T. G. Allen, J. Holovský, A. Vlk, S. De Wolf, *J. Phys. Chem. Lett.* **2022**, *13*, 7702.

[72] S. Zeiske, O. J. Sandberg, N. Zarrabi, C. M. Wolff, M. Raoufi, F. Peña-Camargo, E. Gutierrez-Partida, P. Meredith, M. Stolterfoht, A. Armin, *J. Phys. Chem. Lett.* **2022**, *13*, 7280.

[73] A. Rajagopal, P.-W. Liang, C.-C. Chueh, Z. Yang, A. K.-Y. Jen, *ACS Energy Lett.* **2017**, *2*, 2531.

[74] H. Mehdizadeh-Rad, J. Singh, *ChemPhysChem* **2019**, *20*, 2712.

[75] K. Frohna, M. Anaya, S. Macpherson, J. Sung, T. A. S. Doherty, Y.-H. Chiang, A. J. Winchester, K. W. P. Orr, J. E. Parker, P. D. Quinn, K. M. Dani, A. Rao, S. D. Stranks, *Nat. Nanotechnol.* **2022**, *17*, 190.

[76] D. W. de Quilettes, S. M. Vorpahl, S. D. Stranks, H. Nagaoka, G. E. Eperon, M. E. Ziffer, H. J. Snaith, D. S. Ginger, *Science* **2015**, *348*, 683.

[77] H. Zhou, Q. Chen, G. Li, S. Luo, T. Song, H.-S. Duan, Z. Hong, J. You, Y. Liu, Y. Yang, *Science* **2014**, *345*, 542.

[78] D. Glowienka, Y. Galagan, *Adv. Mater.* **2022**, *34*, 2105920.

[79] P. Caprioglio, C. M. Wolff, O. J. Sandberg, A. Armin, B. Rech, S. Albrecht, D. Neher, M. Stolterfoht, *Adv. Energy Mater.* **2020**, *10*, 2000502.

[80] Z. Sun, G. Sitbon, T. Pons, A. A. Bakulin, Z. Chen, *Sci. Rep.* **2015**, *5*, 10626.

[81] K. W. Kemp, A. J. Labelle, S. M. Thon, A. H. Ip, I. J. Kramer, S. Hoogland, E. H. Sargent, *Adv. Energy Mater.* **2013**, *3*, 917.

[82] F. Gao, Z. Li, J. Wang, A. Rao, I. A. Howard, A. Abrusci, S. Massip, C. R. McNeill, N. C. Greenham, *ACS Nano* **2014**, *8*, 3213.

[83] I. Riedel, J. Parisi, V. Dyakonov, L. Lutsen, D. Vanderzande, J. C. Hummelen, *Adv. Funct. Mater.* **2004**, *14*, 38.

[84] C. Li, S. Tscheuschner, F. Paulus, P. E. Hopkinson, J. Kießling, A. Köhler, Y. Vaynzof, S. Huettner, *Adv. Mater.* **2016**, *28*, 2446.

[85] A. M. A. Leguy, Y. Hu, M. Campoy-Quiles, M. I. Alonso, O. J. Weber, P. Azarhoosh, M. van Schilfgaarde, M. T. Weller, T. Bein, J. Nelson, P. Docampo, P. R. F. Barnes, *Chem. Mater.* **2015**, *27*, 3397.

[86] J. Huang, S. Tan, P. D. Lund, H. Zhou, *Energy Environ. Sci.* **2017**, *10*, 2284.

[87] S. Y. Kwon, B. Kang, J. H. Won, C. Y. Lee, K. Hwang, H. H. Kim, D. Park, W. K. Choi, I. S. Kim, G. Y. Kim, Y. H. Jang, P. Lee, S. H. Im, T. Kim, *Adv. Mater. Interfaces* **2023**, *10*, 2202249.

[88] I. Mesquita, L. Andrade, A. Mendes, *Sol. Energy* **2020**, *199*, 474.

[89] U.-G. Jong, C.-J. Yu, G.-C. Ri, A. P. McMahon, N. M. Harrison, P. R. F. Barnes, A. Walsh, *J. Mater. Chem. A* **2018**, *6*, 1067.

[90] J. A. Christians, P. A. Miranda Herrera, P. V. Kamat, *J. Am. Chem. Soc.* **2015**, *137*, 1530.

[91] A. Hexemer, W. Bras, J. Glossinger, E. Schaible, E. Gann, R. Kirian, A. MacDowell, M. Church, B. Rude, H. Padmore, *J. Phys. Conf. Ser.* **2010**, *247*, 012007.

[92] R. J. Pandolfi, D. B. Allan, E. Arenholz, L. Barroso-Luque, S. I. Campbell, T. A. Caswell, A. Blair, F. De Carlo, S. Fackler, A. P. Fournier, G. Freychet, M. Fukuto, D. Gürsoy, Z. Jiang, H. Krishnan, D. Kumar, R. J. Kline, R. Li, C. Liman, S. Marchesini, A. Mehta, A. T. N'Diaye, D. Y. Parkinson, H. Parks, L. A. Pellouchoud, T. Perciano, F. Ren, S. Sahoo, J. Strzalka, D. Sunday, et al., *J. Synchrotron Radiat.* **2018**, *25*, 1261.

[93] G. Benecke, W. Wagermaier, C. Li, M. Schwartzkopf, G. Flucke, R. Hoerth, I. Zizak, M. Burghammer, E. Metwalli, P. Müller-Buschbaum, M. Trebbin, S. Förster, O. Paris, S. V. Roth, P. Fratzl, *J. Appl. Crystallogr.* **2014**, *47*, 1797.